ACS APPLIED MATERIALS & INTERFACES

Research Article

www.acsami.org

Ternary Spinel MCo_2O_4 (M = Mn, Fe, Ni, and Zn) Porous Nanorods as Bifunctional Cathode Materials for Lithium−O_2 Batteries

Saad Gomaa Mohamed,[†,‡,⊥] Yuan-Quei Tsai,[†,⊥] Chih-Jung Chen,[†] Yi-Ting Tsai,[†] Tai-Feng Hung,[§] Wen-Sheng Chang,[§] and Ru-Shi Liu*[,†,∥]

[†]Department of Chemistry, National Taiwan University, Taipei 106, Taiwan

[‡]Nano Science and Technology Program, Taiwan International Graduate Program, Academia Sinica and National Taiwan University

[§]Energy & Environment Research Laboratories, Industrial Technology Research Institute, Hsinchu 300, Taiwan

[∥]Department of Mechanical Engineering and Graduate Institute of Manufacturing Technology, National Taipei University of Technology, Taipei 106, Taiwan

Supporting Information

ABSTRACT: The development of Li−O_2 battery electrocatalysts has been extensively explored recently. The Co_3O_4 oxide has attracted much attention because of its bifunctional activity and high abundance. In the present study, toxic Co^{2+} has been replaced through the substitution on the tetrahedral spinel A site ions with environmental friendly metals (Mn^{2+}, Fe^{2+}, Ni^{2+}, and Zn^{2+}), and porous nanorod structure are formed. Among these spinel MCo_2O_4 cathodes, the $FeCo_2O_4$ surface has the highest Co^{3+} ratio. Thus, oxygen can be easily adsorbed onto the active sites. In addition, Fe^{2+} in the tetrahedral site can easily release electrons to reduce oxygen and oxidize to half electron filled Fe^{3+}. The $FeCo_2O_4$ cathode exhibits the highest discharging plateau and lowest charging plateau as shown by the charge−discharge profile. Moreover, the porous $FeCo_2O_4$ nanorods can also facilitate achieving high capacity and good cycling performance, which are beneficial for O_2 diffusion channels and Li_2O_2 formation/decomposition pathways.

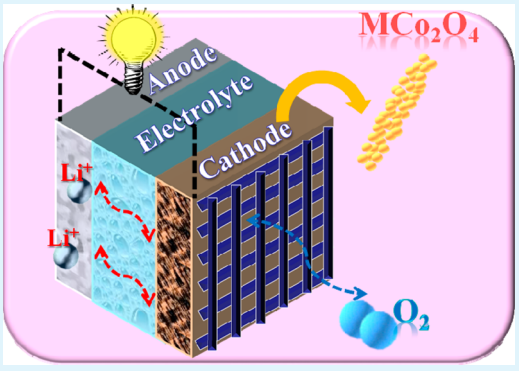

KEYWORDS: *lithium−O_2 batteries, cathode materials, ternary metal oxides, porous nanorods, MCo_2O_4*

1. INTRODUCTION

Renewable energy sources as clean and efficient energy resources have attracted much interest because of the serious concerns regarding the estimated expanding world energy consumption within the next few years.[1] The use of fossil fuels is not the most feasible solution to meet this requirement because of its resulting carbon emission that leads to serious global warming and greenhouse effects. Lithium−air batteries with ultrahigh theoretical energy density comparable to the energy density to gasoline are the best candidates to solve this emergency problem and satisfy the most challenging needs for energy storage in numerous applications.[2−4] These batteries exhibit an energy density of 1700 W h kg^{-1}, which is ten times as much as that of lithium-ion battery (160 W h kg^{-1}). The nonaqueous rechargeable Li−O_2 cell is mainly composed of Li metal as anode, a nonaqueous Li^+-conducting electrolyte, and a porous catalyst as cathode.[5] During the discharging process, the Li anode is oxidized to ions (Li^+) and diffused through the electrolyte to the catalyst cathode material. The electrons are simultaneously conducted from the outer circuit, and oxygen gas is reduced to generate O^{2-} ions. The Li^+ ions further react with O^{2-} ions to form Li_2O_2 to complete the discharging step. By contrast, the charging process of lithium−air batteries is subjected to the reversed chemical reaction. The essential electrochemical reactions are presented as follows: anode, $Li \leftrightarrow Li^+ + e^-$, and cathode, $2Li^+ + 2e^- + O_2 \leftrightarrow Li_2O_2$ (E_0 = 2.96 V vs Li/Li^+).[6]

Noble metals with high conductivity, as well as excellent oxygen evolution and reduction reaction activities, are the most commonly studied cathode materials. Carbon materials have been developed to reduce cost by avoiding the use of these precious metals. However, these carbon materials are limited by their low oxygen evolution reaction (OER) and deteriorating capacity caused by Li_2O_2 formation during cycling in an organic electrolyte.[7] Metal oxides have been extensively explored as cathode catalysts for Li−O_2 batteries because of their high abundance, low cost, and catalytic abilities for oxygen reduction reaction (ORR) and OER (bifunctional activities). Various metal oxides, such as Fe_2O_3, Fe_3O_4, NiO, CuO, and Co_3O_4 have been investigated as cathode catalysts.[8] Co_3O_4, as a potential cathode catalyst, exhibits not only high capacitance of approximately 2000−3000 mA h g^{-1}, but also high capacity

Received: March 12, 2015
Accepted: May 18, 2015
Published: May 18, 2015

DOI: 10.1021/acsami.5b02180
ACS Appl. Mater. Interfaces 2015, 7, 12038−12046

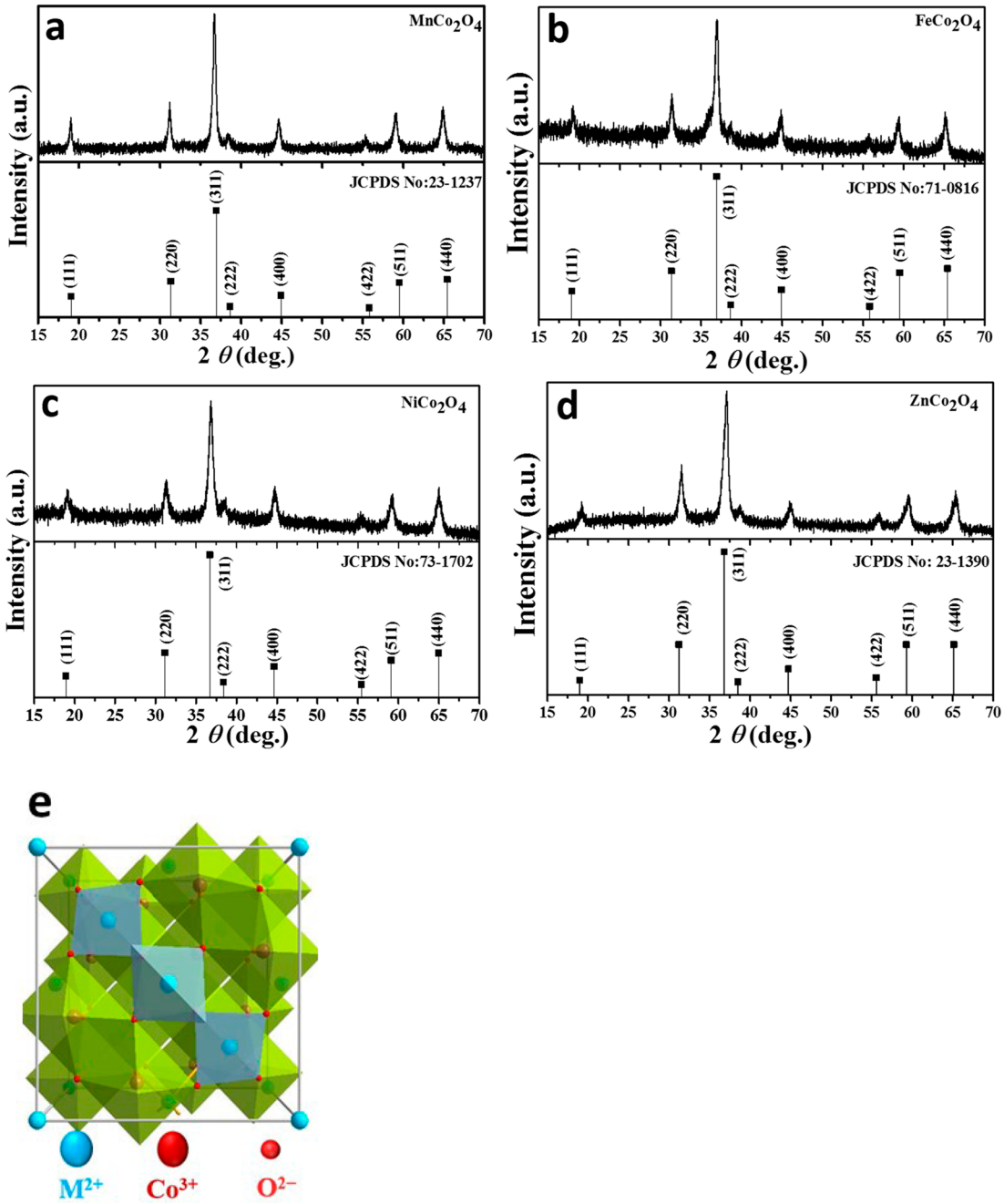

Figure 1. XRD patterns of different metal cobalt oxides (a) $MnCo_2O_4$, (b) $FeCo_2O_4$, (c) $NiCo_2O_4$, and (d) $ZnCo_2O_4$. (e) Schematic diagram of spinel structure.

retention rate and good bifunctional catalytic ability.[9,10] However, Co^{2+} is poisonous and hazardous to the environment. Therefore, more environmentally friendly metal ions have been considered to substitute Co^{2+} and thereafter enhance its conductivity.[11] Wang et al.[12] first attempted to use ternary MCo_2O_4 for Li−O_2 battery cathode. They demonstrated the substitution of toxic Co^{2+} ions in spinel Co_3O_4 structure with environmental friendly Mn^{2+} ions to form $MnCo_2O_4$ nanoparticles. In addition, they also decorated $MnCo_2O_4$ with graphene supports to improve poor conductivity. Several porous ternary MCo_2O_4 structures, including $NiCo_2O_4$ nanoflakes, $ZnCo_2O_4$ nanoflakes, and MnCo2O4 microspheres, were also prepared to further enhance the catalytic activity of MCo_2O_4.[13−15]

However, the influence of Co^{2+} replacement in the Co_3O_4 matrix by M^{2+} (Mn^{2+}, Fe^{2+}, Ni^{2+}, and Zn^{2+}) on the improvement of the corresponding catalytic performance has not been fully elucidated. Therefore, in this study, the effect of Co^{2+} ion substitution on catalytic behavior of the Li−O_2 battery cathode has been evaluated. $MnCo_2O_4$, $FeCo_2O_4$, $NiCo_2O_4$, and $ZnCo_2O_4$ nanorods were synthesized by a facile hydrothermal method. These structures are porous, which improves the capacity and cycling performance. Moreover, they provide channels for O_2 diffusion and more voids to store the discharging products, including Li_2O_2. Consequently, the capacity and maintenance of suitable reaction interfaces during the discharge−charge process can be achieved by improving the reversibility of the lithium−O_2 battery.

DOI: 10.1021/acsami.5b02180
ACS Appl. Mater. Interfaces 2015, 7, 12038−12046

2. EXPERIMENTAL SECTION

2.1. Preparation of MCo_2O_4 (M = Mn, Fe, Ni, and Zn) Porous Nanorods. Metal nitrates (1 mmol) and cobalt nitrate (2 mmol) were first dissolved in 25 mL deionized water. Then, urea (5 mmol) and ammonium fluoride (2 mmol) were dissolved in 25 mL deionized water. The two solutions were homogeneously mixed by ultrasonication for 0.5 h. The mixed solution was then transferred into Teflon-lined stainless steel autoclave. The autoclave was sealed and placed in an oven at 140 °C for 7 h. After the hydrothermal reaction, the autoclave was left to cool down to room temperature. The products were filtered, washed with deionized water and ethanol to remove the residues, and finally dried. The dried powders were then ground and calcined at 400 °C for 2 h under air atmosphere, yielding porous MCo_2O_4 nanorods.

2.2. Characterizations. The crystal structures of the porous MCo_2O_4 (M = Mn, Fe, Ni, and Zn) nanorods were examined by an X-ray diffractometer (Bruker D2 PHASER) with a Cu Kα (λ = 1.541 Å) radiation. The measurements were conducted over the scanning angle range of 2θ = 10°−75°. For morphological clarifications, a field-emission scanning electron microscope (JEOL JSM-6700F, with EDS instruments) and a high-resolution transmission electron microscope (HRTEM, JEOL JEM-2100F) were utilized. The Brunauer−Emmett−Teller (BET) surface area was determined from nitrogen adsorption−desorption isotherms at 77 K (Micrometrics ASAP 2020 V3.00 H) with an accelerated surface area and porosimetry system. The chemical compositions were confirmed using X-ray photoelectron spectroscopy (XPS, PHI Quantera) with a monochromatic Al Kα (λ = 8.3406 Å) radiation source. Co K-edge X-ray absorption near edge structure (XANES) spectra were collected at BL01C1 beamline of the National Synchrotron Radiation Research Center. The catalytic activity was confirmed by CV testing with MCo_2O_4 nanorod-coated glassy carbon (MCO-GC covered by 20 μL of 0.05 wt % Nafion solution) as the working electrode, Li foils as counter and reference electrodes, and 1 M O_2-saturated bistrifluoromethanesulfonimidate/tetraethylene glycol dimethyl ether (LiTFSI/TEGDME) as an electrolyte. The rotating speed of the electrocatalyst-coated GC electrode was kept at 1600 rpm by a compact pine rotator (AFMSRCE, PINE Instrument).

2.3. Li−O_2 Battery Measurements. The homogeneous slurry was composed of porous MCo_2O_4 (M = Mn, Fe, Co, Ni, and Zn) nanorods, Super P as a conductive additive, and poly-(vinylidenedifluoride) (PVDF) as a binder in a weight ratio of 60:20:20. Then, the prepared slurry was coated onto stainless steel mesh substrate as current collector. The cathode containing pure carbon with 80 wt % Super P and 20 wt % PVDF was also prepared under the same processes for comparison. A typical total loading weight of the cathode material on an active area of 1 cm^2 was approximately 4−5 mg cm^{-2}. The coin- type (CR2032) Li−O_2 batteries were assembled inside a glovebox using Li foil as anode, 1 M lithium LiTFSI/TEGDME as an electrolyte, and a glass fiber as a separator. The batteries were fixed in a dry vessel with desiccants added, and 100 mL min^{-1} of oxygen was continuously fed through a mass flow controller (Model GFC 17, AALBORG Instruments and Controls, Inc.).[14] All of the measurements were conducted with a computer-controlled workstation (BAT 750B, AcuTech systems Co., Ltd.) between the potential range of 2.3 and 4.3 V vs Li/Li^+ at a constant current density of 0.1 mA cm^{-2}. The obtained results were normalized by the weight of carbon presented in the cathode for capacity comparison in this study. The EIS measurements were performed using an electrochemical workstation (AUTOLAB PGST30, Eco Chemie) in the frequency range of 1 MHz to 1 Hz (amplitude of 5 mV). The EIS data were analyzed using Nyquist plots.

3. RESULTS AND DISCUSSION

Different metal cobalt oxides were prepared by urea-assisted hydrothermal method. Figures 1a to d show that the X-ray diffraction (XRD) spectra of MCo_2O_4 (M = Mn, Fe, Ni, and Zn). MCo_2O_4 nanorods were successfully synthesized with no impurity phase after the hydrothermal reaction and heat treatment. MCo_2O_4 revealed the peaks of (111), (220), (311), (222), (400), (422), (511), and (440), which was identified as spinel ($MnCo_2O_4$ JCPDS file no. 23-1237, $FeCo_2O_4$ consistent with Co_3O_4, JCPDS file no. 71-0816 and previous reports,[16−18] $NiCo_2O_4$ JCPDS file no. 73-1702, and $ZnCo_2O_4$ JCPDS file no. 23-1390, all with space group $Fd3m$). This result indicates that M^{2+} ions successfully replaced Co^{2+} in the spinel tetrahedral A sites together with Co^{3+} in spinel structure B octahedral hole sites (Figure 1e). To analyze the crystal lattices of MCo_2O_4, Rietveld refinement based on XRD data was carried out (Figure S1, Supporting Information) and the crystallographic parameters are shown in Table S1 (Supporting Information).

Figure 2 and Figure S2 (Supporting Information) show the morphology of the MCo_2O_4. The scanning electron micrographs of the four kinds of metal cobaltite oxides clearly revealed the nanorod structure. The nanorod of corresponding metal oxides is composed of many nanoparticles, causing numerous voids between the particles. Energy-dispersive X-ray spectrometry (EDS) microanalysis of the MCo_2O_4 (Figure S3, Supporting Information) displays that the nanorods comprise M (Mn, Fe, Ni and Zn), Co, and O elements with atomic ratio of almost of 1:2:4, indicating the formation of pure MCo_2O_4. The transmission electron micrographs in Figure 3 illustrate that the mesoporous structure is generated by heat treatment in air during synthesis. The metal hydroxide product reacted with O_2 to release CO_2 and H_2O, resulting in small pores.[18,19] The porous structure facilitated the flow of oxygen and the electrolyte inside the catalyst material, providing and maintaining an appropriate and two-phase interface (O_2 first dissolves in the electrolyte and participates in the actual ORR charge-transfer reaction)[20,21] leading to enhanced catalytic activity. Spaces for lithium peroxide storage also formed during discharge, which improved the cyclability. The voids also reduced the formation of discharge products that can clog the surface of the catalyst materials, leading to the maintenance of the catalyst interface to assist lithium peroxide decomposition and improvement of the life cycle of lithium−O_2 batteries. The HRTEM images shown in Figure S4 (Supporting Information) clearly show the mesoporous nature of the products (highlighted by red color). The resolved lattice fringes shown in

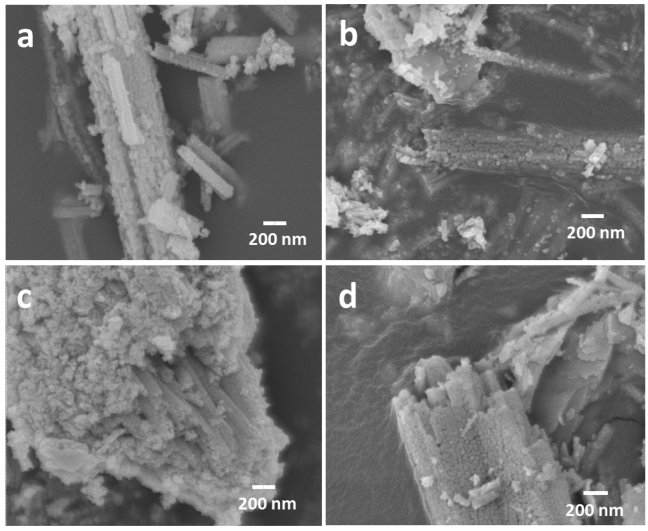

Figure 2. Scanning electron micrographs of (a) $MnCo_2O_4$, (b) $FeCo_2O_4$, (c) $NiCo_2O_4$, and (d) $ZnCo_2O_4$.

DOI: 10.1021/acsami.5b02180
ACS Appl. Mater. Interfaces 2015, 7, 12038−12046

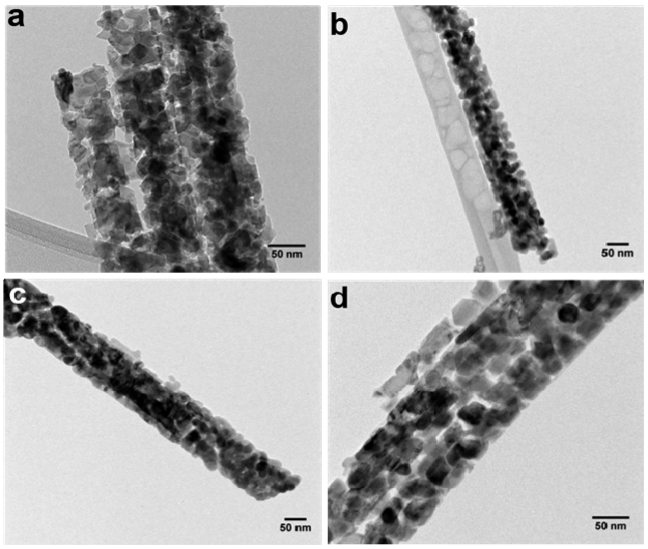

Figure 3. Transmission electron micrographs of (a) $MnCo_2O_4$, (b) $FeCo_2O_4$, (c) $NiCo_2O_4$, and (d) $ZnCo_2O_4$.

Figure S4 (Supporting Information) are approximately 0.24, 0.29, and 0.46 nm, which can be appointed to the (311), (220), and (111) planes of the MCo_2O_4 spinel phase. This result further confirms the formation of crystalline phase metal oxides. This finding is consistent with the XRD pattern and further confirmed by the corresponding selected area electron diffraction pattern shown in Figure S5 (Supporting Information), which also shows the polycrystalline nature for the produced MCo_2O_4.

The porous characteristics of metal oxide samples were also examined by nitrogen adsorption and desorption measurement. Nitrogen adsorption−desorption isotherm and the corresponding Barrett−Joyner−Halenda (BJH) pore size distribution plots of MCo_2O_4 are displayed in Figure 4. All adsorption isotherms of $MnCo_2O_4$, $FeCo_2O_4$, $NiCo_2O_4$, and $ZnCo_2O_4$ are similar and could be categorized as type-V and H3 loop type isotherms. Type-V is usually obtained with certain porous adsorbents, although this kind of isotherm type is uncommon. The H3 hysteresis loops are typically observed in aggregates of platelike particles resulting in slit-shaped mesopores.[22] The mesoporosity and the wide pore size distribution are consistent with the TEM images. The BET specific surface areas of $MnCo_2O_4$, $FeCo_2O_4$, $NiCo_2O_4$, and $ZnCo_2O_4$ are 40.4, 66.8, 73.9, and 46.7 $m^2\ g^{-1}$, respectively, but without significant differences among these cathode materials. The pore size distribution range from 2 to 50 nm (BJH inset graph of Figure 4). The BET results are consistent with the TEM observations, confirming the mesoporous characteristics of the products.

De Koninck et al. reported that the electronegative O_2 adsorbs strongly by increasing Co^{3+} octahedral species resulted from the partial substitution of the Co^{2+} ion by the M^{2+} ion, leading to an increased surface Co^{3+}/Co^{2+} ratio (the Co^{3+}−O bond is stronger than the Co^{2+}−O bond).[23] Oxygen then tends to adsorb on the Co_3^+ surface and become the main active sites in ORR in the 1 M KOH electrolyte.[23] Therefore, the effect of different Co^{3+}/Co^{2+} by M^{2+} substitution on the catalytic activity of the produced ternary metal oxides (MCo_2O_4) as Li−O_2 battery cathode should be determined. XANES spectra of different MCo_2O_4 are shown in Figure 5a. The Co K-edge (Figure 5b) absorption shows that all oxidation states of MCo_2O_4 are similar to those of commercial Co_3O_4, which are composed of both Co^{2+} and Co^{3+} species, indicating the similarity chemical environment of the bulk metal oxides.

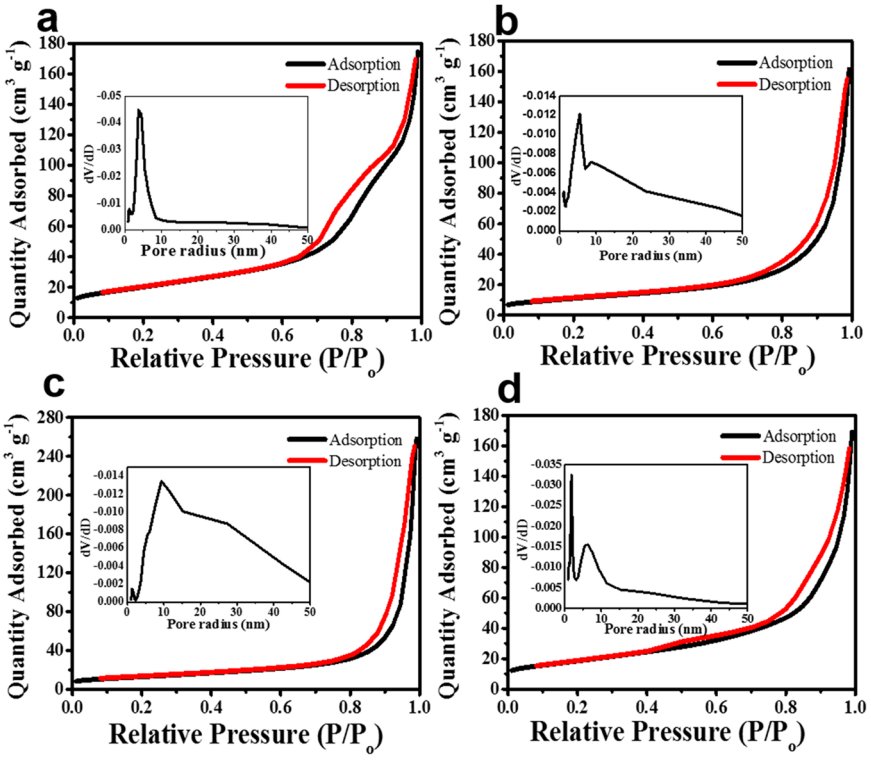

Figure 4. N_2 adsorption−desorption isotherms of (a) $MnCo_2O_4$, (b) $FeCo_2O_4$, (c) $NiCo_2O_4$, and (d) $ZnCo_2O_4$. The inset is the pore size distribution of the different metal cobalt oxides.

DOI: 10.1021/acsami.5b02180
ACS Appl. Mater. Interfaces 2015, 7, 12038−12046

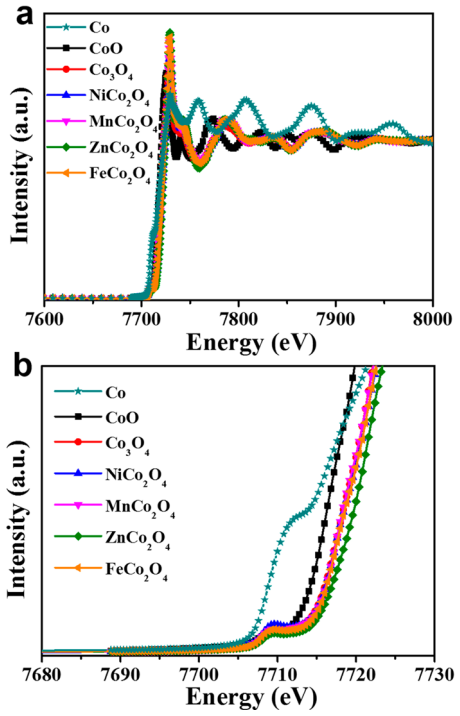

Figure 5. (a) XAS spectrum and (b) absorption edges of the different metal cobalt oxides.

However, these results do not provide appropriate description for the electrochemical process.

Given that the catalytic activity is mainly a surface phenomenon,[24] surface sensitive XPS measurement is used to characterize the valence of MCo_2O_4 cathodes. The full wide-scan XPS spectra of all MCo_2O_4 are shown in Figure S6 (Supporting Information), revealing the purity of the produced metal oxide. Figure S6 reveals also that the atomic ratio of M/Co is approximately 0.5, which corresponds to the surface chemical composition as MCo_2O_4. The peak deconvolution and fitting were carried out using Gaussian−Lorentzian shaped peaks based on the Shirley background correction. Figures 6a−d show the XPS spectra of Mn 2p, Fe 2p, Ni 2p, and Zn 2p, respectively. In Figure 6a, two peaks are observed at 641.4 and 652.8 eV, and other two peaks are at 643.4 and 653.7 eV of Mn $2p_{3/2}$ and Mn $2p_{1/2}$ spin−orbit coupling, which could be ascribed to Mn^{2+} and Mn^{3+}, respectively.[25] This result indicates that the manganese in $MnCo_2O_4$ is Mn^{2+} and Mn^{3+} mixed-valence. Figure 6b shows the Fe 2p spectrum in which two peaks are observed at 710.8 and 724.3 eV, which can be attributed to spin−orbit peaks of the Fe $2p_{3/2}$ and Fe $2p_{1/2}$. A "shoulder" satellite peak is found at 715.3, which could be characterized to Fe^{2+},[18,26] indicating that Fe^{2+} is the main species present in $FeCo_2O_4$ surface. Figure 6c shows the Ni 2p XPS spectrum, in which the two observed peaks of Ni $2p_{3/2}$ and Ni $2p_{1/2}$ at 854.1 and 871.9 eV are ascribed to Ni^{2+}. However, the two observed peaks at 855.9 and 873.8 eV are ascribed to the Ni^{3+} oxidation state, also two shakeup type satellite peaks of nickel observed at the high binding energy side of the Ni $2p_{3/2}$ and Ni$2p_{1/2}$ edge observed at around 861.3 and 880.2 eV,[27] indicating that the nickel in $NiCo_2O_4$ is also mixed valence.

Figure 6d shows the XPS spectrum of Zn 2p, with two peaks of Zn $2p_{3/2}$ and Zn $2p_{1/2}$ at 1021.1 and 1044.2 eV, which can be characterized to Zn^{2+} oxidation state.[28] The XPS spectra of cobalt 2p in MCo_2O_4 (M = Ni, Fe, Ni, and Zn) are shown in Figure 7. Figure 7a shows the peaks of Co $2p_{3/2}$ and Co $2p_{1/2}$ of $MnCo_2O_4$. These two peaks can be fitted to two peaks at 780.1 and 795.4 eV, can be ascribed to Co^{3+}, and other two peaks at 782.5 and 797.5 eV, can be ascribed to Co^{2+}. These results indicate the coexistence of the Co(II) and Co(III) in $MnCo_2O_4$ (Co^{3+}/Co^{2+} ratio = 2.4, estimated from the corresponding peaks areas). Figure 7b shows the peaks of Co $2p_{3/2}$ and Co

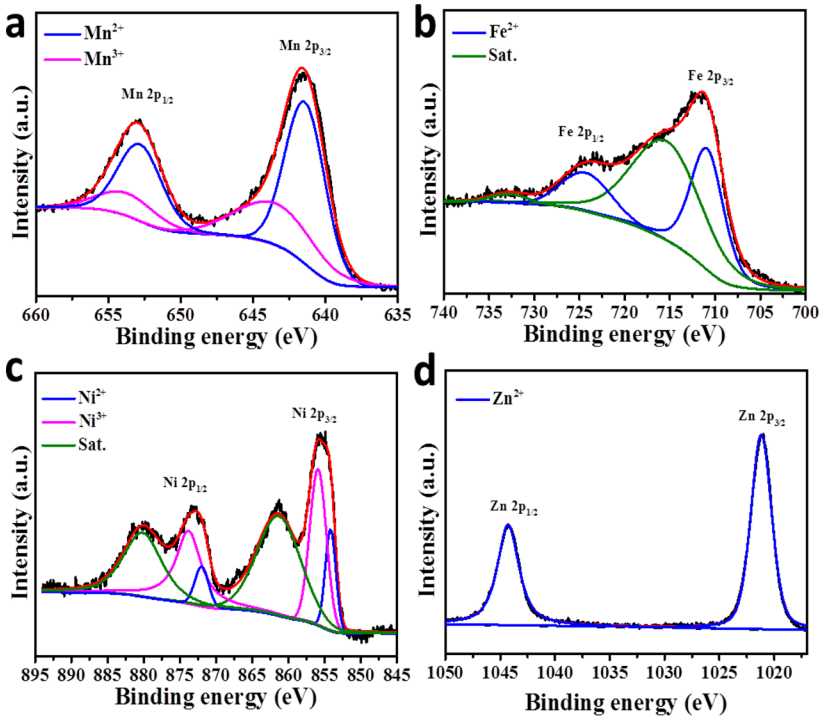

Figure 6. XPS of (a) Mn 2p orbital in $MnCo_2O_4$, (b) Fe 2p orbital in $FeCo_2O_4$, (c) Ni 2p orbital in $NiCo_2O_4$, and (d) Zn 2p orbital in $ZnCo_2O_4$.

DOI: 10.1021/acsami.5b02180
ACS Appl. Mater. Interfaces 2015, 7, 12038−12046

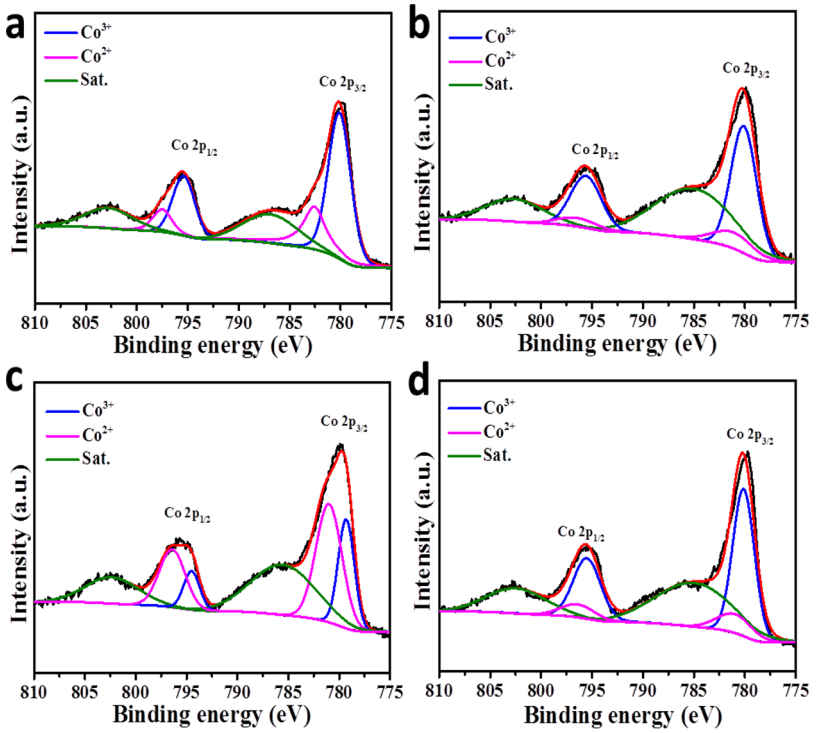

Figure 7. XPS of Co 2p orbital for (a) $MnCo_2O_4$, (b) $FeCo_2O_4$, (c) $NiCo_2O_4$, and (d) $ZnCo_2O_4$.

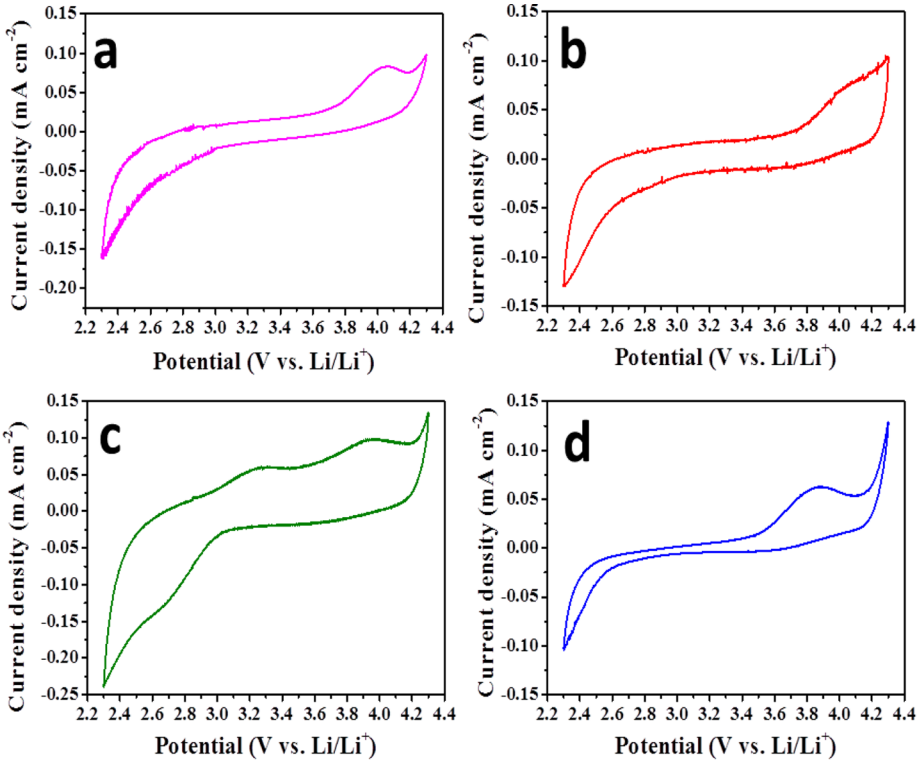

Figure 8. CV curves of (a) $MnCo_2O_4$, (b) $FeCo_2O_4$, (c) $NiCo_2O_4$, and (d) $ZnCo_2O_4$ in TEGDME electrolyte containing 1 M LiTFSI at a scan rate of 5 mV s^{-1}.

$2p_{1/2}$ of $FeCo_2O_4$, the fitted peaks at 780.1 and 795.5 eV are consistent with Co^{3+}. By contrast, the peaks at 781.1 and 796.4 eV (weak intensity values) are consistent with Co^{2+}. This result indicates the coexistence of the Co(II) and Co(III), although only Fe^{2+} is observed on $FeCo_2O_4$, suggesting that Fe^{2+} did not fully substitute Co^{2+}. However, the absence of Fe^{3+} might increase Co^{3+} ratio (Co^{3+}/Co^{2+} ratio = 4.9, estimated from the corresponding peaks areas).

Figure 7c shows the peaks of Co $2p_{3/2}$ and Co $2p_{1/2}$ of $NiCo_2O_4$. The fitted peaks at 779.3 and 794.5 eV are ascribed to Co^{3+}, and the fitted peaks at 781.0 and 796.4 eV are ascribed to Co^{2+}, indicating the cobalt of $NiCo_2O_4$ is also a mixed-

DOI: 10.1021/acsami.5b02180
ACS Appl. Mater. Interfaces 2015, 7, 12038−12046

valence (Co^{3+}/Co^{2+} ratio = 0.6, estimated from the corresponding peaks areas). Figure 7d shows the peaks of Co $2p_{3/2}$ and Co $2p_{1/2}$ of $ZnCo_2O_4$, the fitted peaks at 780.1 and 795.5 eV are indexed to Co^{3+}, and the fitted peaks at 781.0 and 796.4 eV are attributed to Co^{2+}, (Co^{3+}/Co^{2+} ratio = 4.7).[25,27,28] Therefore, these results imply that both $FeCo_2O_4$ and $ZnCo_2O_4$ are more active because of their higher Co^{3+}/Co^{2+} ratio (4.9 and 4.7), to which oxygen could strongly adsorb. The O 1s XPS spectrum (Figure S7, Supporting Information) for all MCo_2O_4 displays two main peaks at approximately 529 (corresponding to a characteristic bond between metal and oxygen) and at 531 eV, which corresponds to some defect sites with low oxygen coordination in the structure.[27] All XPS binding energies, FHWM, distance between $2p_{3/2}$ and $2p_{1/2}$ and satellites position of Co and M in MCo_2O_4 are listed in Table S2 (Supporting Information).

Evaluation of the electrocatalytic activities of different metal oxides using the CV test was first recorded. The activities were measured in 1 M O_2-saturated LiTFSI/TEGDME electrolyte at a scan rate of 5 mV s^{-1}. All MCo_2O_4 (M = Mn, Fe, Ni, and Zn) CV curves are shown in Figure 8. In the CV curves, the OER anodic and ORR cathodic peaks obviously appeared, compared with pure Super P CV behavior shown in Figure S8 (Supporting Information). The CV behavior indicates that these ternary metal oxides are effective for both ORR/OER activities. The results are confirmed with the voltage profiles of the first discharge−charge cycle of Li−O_2 batteries plotted in Figure 9. Figure 9 displays first capacity−voltage profiles of Li−

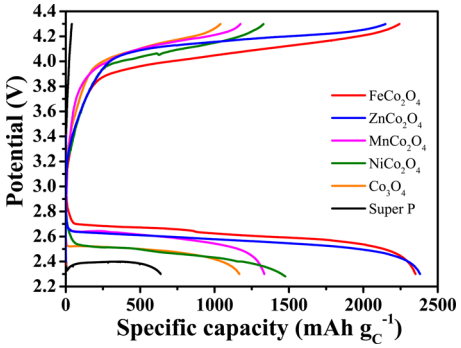

Figure 9. Voltage profiles of the first discharge−charge cycle of Li−O_2 batteries using the different metal cobalt oxide-based electrodes and the Super P-based electrode as cathodes at 0.1 mA cm^{-2}.

O_2 batteries of all MCo_2O_4 mesoporous nanorods and Super P-based cathodes tested from 2.3 to 4.3 V (vs Li/Li^+) using 0.1 mA cm^{-2} current density.

The discharge and charge plateau voltages, as well as the capacities, of Co_3O_4, $MnCo_2O_4$, $FeCo_2O_4$, $NiCo_2O_4$, and $ZnCo_2O_4$ are listed in Table 1. Given that Super P has poor OER catalytic activity, which corresponds to the CV results, a stable charging plateau cannot be maintained (Figure 9). The reduced discharging overpotential (increasing the discharging voltage and decreasing the charging voltage) and the increased capacity compared with Co_3O_4 are observed. The capacity of $FeCo_2O_4$ $ZnCo_2O_4$, $MnCo_2O_4$, and $NiCo_2O_4$ cathodes are 2350.0, 2381.7, 1334.9, and 1491.6 mA h g_c^{-1}, respectively. Because of the high ratio of Co^{3+}/Co^{2+}, in case of the $FeCo_2O_4$ cathode, oxygen can easily adsorb onto an active site, leading to higher discharging plateau voltage (2.67 V vs Li/Li^+, lower discharge overpotential) and higher capacity compared with other MCo_2O_4 cathodes (the capacity value closes to

Table 1. Performance of the Different Metal Cobalt Oxide-Based Electrodes

	discharge plateau (V)	charge plateau (V)	capacity (mA h g_c^{-1})
$FeCo_2O_4$	2.67	3.96	2350.0
$ZnCo_2O_4$	2.61	4.08	2381.7
$MnCo_2O_4$	2.61	4.10	1334.9
$NiCo_2O_4$	2.50	4.03	1491.6
Co_3O_4	2.50	4.10	1166.6
Super P	2.38		638.2

$ZnCo_2O_4$). $FeCo_2O_4$ cathode also exhibits lower charge plateau voltage of 3.96 V vs Li/Li^+, lower charge overpotential, indicating its excellent performance in the Li−O_2 battery cathode.

In addition, Fe^{2+} is easy to oxidase to the half-filled d orbital Fe^{3+},[29,30] which may cause the surface of $FeCo_2O_4$ to provide electron for oxygen reduction, leading to catalytic activity enhancement. This condition may have resulted in the smaller overpotential of $FeCo_2O_4$ than that of $ZnCo_2O_4$. A similar procedure was applied to study the cycling performances for MCo_2O_4 nanorod-based cathodes for Li−O_2 battery.

As compared in the Nyquist plots (Figure S9, Supporting Information), the interfacial resistance, which includes the contributions from charge transfer resistance and Li ion transport resistance through passivation layers, after discharge and recharging process for all MCo_2O_4 electrodes became slight larger than before electrochemical cycling, indicating the stability of the electrodes after electrochemical cycles, particularly in the case of $FeCo_2O_4$ and $ZnCo_2O_4$.

The cycling performances are displayed in Figure 10. Using a cutoff capacity of 500 mA h g^{-1}, all cathodes ran steadily for 40 cycles of discharge and charge, which can be indicated to the cathode bifunctional electrocatalytic activities. The mesoporous structure of MCo_2O_4 can assist the flows of oxygen and electrolyte to prevent channel clogging by discharge products and, also, ensure the accommodation of a large amount of discharge products and to facilitate rapid mass (oxygen and lithium ions);[31] moreover, the porous structure of MCo_2O_4 nanorods, which maximizes the availability of the catalytic sites and facilitates the transport of electrons and O_2, thus decreases the overpotential by polarization.[15] The first cycle of charging plateau is higher than the successive cycles, probably because of the slow initial reaction kinetics of Li_2O_2 dissociation, which became faster by catalysis activation during the subsequent cycles.

For further investigation of excellent electrochemical performance of MCo_2O_4 nanorods electrode, the discharge and recharge products in the $FeCo_2O_4$ nanorods-based cathode of Li−O_2 batteries, which exhibited the best performance, are analyzed by ex situ SEM. The SEM images of the pristine, after first discharge (to 2.3 V) and after recharge (to 4.3 V) of $FeCo_2O_4$ nanorods electrode are shown in Figures S10a−c (Supporting Information), respectively. Before discharge, the mesoporous $FeCo_2O_4$ nanorods and Super P carbon nanoparticles are observed in the as-prepared cathode (Figure S10a, Supporting Information). After discharge, nanosheets are observed on the surface of cathode, which are considered as aggregates comprised of nanocrystalline Li_2O_2 (Figure S10b and its highly magnified Figure S11, Supporting Information). The nanosheets morphology of Li_2O_2 was also observed in previous works.[15,31,32] A possible formation mechanism of the

DOI: 10.1021/acsami.5b02180
ACS Appl. Mater. Interfaces 2015, 7, 12038−12046

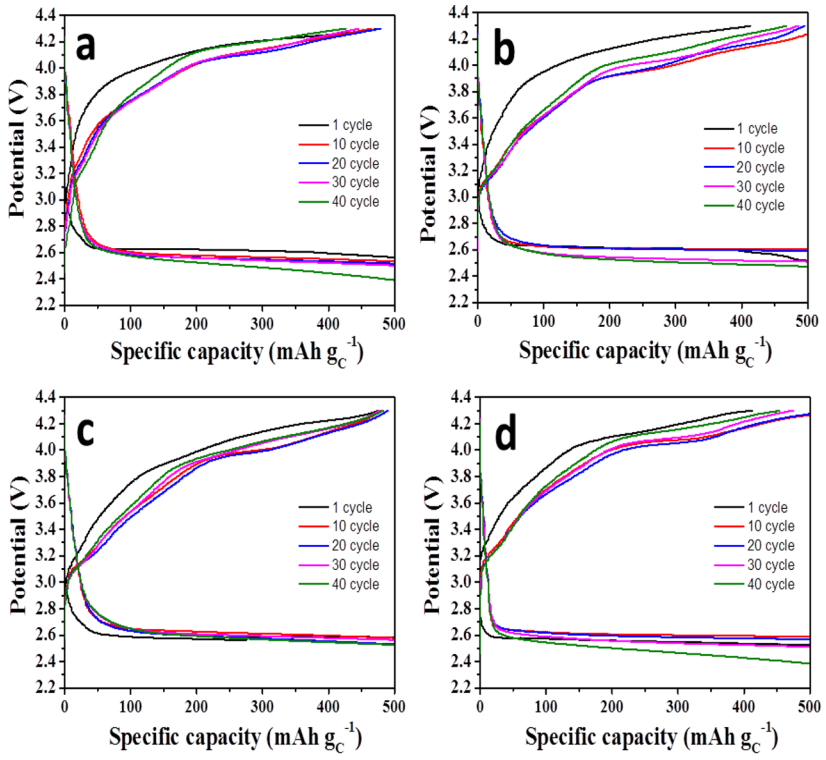

Figure 10. Profiles of a Li−O_2 battery using (a) $MnCo_2O_4$-, (b) $FeCo_2O_4$-, (c) $NiCo_2O_4$-, and (d) $ZnCo_2O_4$-based electrodes at different discharge−charge cycles.

Li_2O_2 aggregated products is that the hexagonal crystal structure of the Li_2O_2 and preferred nucleation on the prismatic crystal faces may give rise to toroidal and other shape aggregates of Li_2O_2 nanocrystallites[33] (Figure S10b and Figure S11, Supporting Information). The Li_2O_2 particles obviously disappeared during the following charge process (Figure S10c, Supporting Information), suggesting a highly reversible process of the electrode.

4. CONCLUSIONS

In summary, porous MCo_2O_4 (M = Mn, Fe, Ni, and Zn) nanorods as cathode materials for lithium−O_2 batteries were prepared through a facile hydrothermal reaction. The mesoporous structure enabled the flow of oxygen and electrolyte during discharge reaction and provided good two-phase interface for catalysis. This structure also provided additional storage space for lithium peroxide and improved the capacity. Additionally, it also helped avoid the discharge products covering the surface of the catalyst, leading to the unclogging of O_2 pathways and decomposition of discharge products. Thus, the battery was stable for 40 cycles. A lower overpotential and higher capacity of spinel MCo_2O_4 were correspondingly resulted compared with those of commercial Co_3O_4. $FeCo_2O_4$ cathode exhibited higher capacity and lower overpotential, because of the higher Co^{3+}/Co^{2+} ratio, which led to the high O_2 absorption to the catalytic surface. Thus, the more electropositive Co^{3+} ions functioned as active sites to adsorb the oxygen molecules. Therefore, MCo_2O_4 with higher amount of Co^{3+} ions result in better electrochemical performance.

■ ASSOCIATED CONTENT

Ⓢ Supporting Information

HRTEM images, SEAD patterns, full-range XPS spectrum, O 1s XPS spectrum, CV curve of Super P, and ex situ SEM. The Supporting Information is available free of charge on the ACS Publications website at DOI: 10.1021/acsami.5b02180.

■ AUTHOR INFORMATION

Corresponding Author

*E-mail: rsliu@ntu.edu.tw. Tel.: +886-2-3366116. Fax.: +886-2-3366 8671.

Author Contributions

⊥S.G.M. and Y.Q.T. contributed equally.

Notes

The authors declare no competing financial interest.

■ ACKNOWLEDGMENTS

We gratefully appreciate the financial support from the Bureau of Energy (BOE), Ministry of Economy Affair (MOEA), Taiwan (103-D0114).

■ REFERENCES

(1) Mirzaeian, M.; Hall, P. J. Characterizing Capacity Loss of Lithium Oxygen Batteries by Impedance Spectroscopy. *J. Power Sources* **2010**, *195*, 6817−6824.

(2) Girishkumar, G.; McCloskey, B.; Luntz, A. C.; Swanson, S.; Wilcke, W. Lithium−Air Battery: Promise and Challenges. *J. Phys. Chem. Lett.* **2010**, *1*, 2193−2203.

(3) Cao, R.; Lee, J.-S.; Liu, M.; Cho, J. Recent Progress in Non-Precious Catalysts for Metal-Air Batteries. *Adv. Energy Mater.* **2012**, *2*, 816−829.

(4) Wang, X.; Zhu, D.; Song, M.; Cai, S.; Zhang, L.; Chen, Y. A Li−O_2/Air Battery Using an Inorganic Solid-State Air Cathode. *ACS Appl. Mater. Interfaces* **2014**, *6*, 11204−11210.

DOI: 10.1021/acsami.5b02180
ACS Appl. Mater. Interfaces 2015, 7, 12038−12046

(5) Peng, Z.; Freunberger, S. A.; Chen, Y.; Bruce, P. G. A Reversible and Higher-Rate Li-O_2 Battery. *Science* **2012**, *337*, 563−566.
(6) Shao, Y.; Park, S.; Xiao, J.; Zhang, J.-G.; Wang, Y.; Liu, J. Electrocatalysts for Nonaqueous Lithium−Air Batteries: Status, Challenges, and Perspective. *ACS Catal.* **2012**, *2*, 844−857.
(7) Etacheri, V.; Sharon, D.; Garsuch, A.; Afri, M.; Frimer, A. A.; Aurbach, D. Hierarchical Activated Carbon Microfiber (ACM) Electrodes for Rechargeable Li-O_2 Batteries. *J. Mater. Chem. A* **2013**, *1*, 5021−5030.
(8) Débart, A.; Bao, J.; Armstrong, G.; Bruce, P. G. An O_2 Cathode for Rechargeable Lithium Batteries: The Effect of a Catalyst. *J. Power Sources* **2007**, *174*, 1177−1182.
(9) Kim, K.; Park, Y. Catalytic Properties of Co_3O_4 Nanoparticles for Rechargeable Li/Air Batteries. *Nanoscale Res. Lett.* **2012**, *7*, 1−6.
(10) Cui, Y.; Wen, Z.; Sun, S.; Lu, Y.; Jin, J. Mesoporous Co_3O_4 with Different Porosities as Catalysts for the Lithium−Oxygen Cell. *Solid State Ionics* **2012**, *225*, 598−603.
(11) Zhang, G.; Lou, X. W. General Solution Growth of Mesoporous $NiCo_2O_4$ Nanosheets on Various Conductive Substrates as High-Performance Electrodes for Supercapacitors. *Adv. Mater.* **2013**, *25*, 976−9.
(12) Wang, H.; Yang, Y.; Liang, Y.; Zheng, G.; Li, Y.; Cui, Y.; Dai, H. Rechargeable Li-O2 Batteries with a Covalently Coupled $MnCo_2O_4$-Graphene Hybrid as an Oxygen Cathode Catalyst. *Energy Environ. Sci.* **2012**, *5*, 7931−7935.
(13) Zhang, L.; Zhang, S.; Zhang, K.; Xu, G.; He, X.; Dong, S.; Liu, Z.; Huang, C.; Gu, L.; Cui, G. Mesoporous $NiCo_2O_4$ Nanoflakes as Electrocatalysts for Rechargeable Li-O_2 Batteries. *Chem. Commun.* **2013**, *49*, 3540−3542.
(14) Hung, T. F.; Mohamed, S. G.; Shen, C. C.; Tsai, Y. Q.; Chang, W. S.; Liu, R. S. Mesoporous $ZnCo_2O_4$ Nanoflakes with Bifunctional Electrocatalytic Activities toward Efficiencies of Rechargeable Lithium-Oxygen Batteries in Aprotic Media. *Nanoscale* **2013**, *5*, 12115−12119.
(15) Ma, S.; Sun, L.; Cong, L.; Gao, X.; Yao, C.; Guo, X.; Tai, L.; Mei, P.; Zeng, Y.; Xie, H.; Wang, R. Multiporous $MnCo_2O_4$ Microspheres as an Efficient Bifunctional Catalyst for Nonaqueous Li−O2 Batteries. *J. Phys. Chem. C* **2013**, *117*, 25890−25897.
(16) Ferreira, T. A. S.; Waerenborgh, J. C.; Mendonça, M. H. R. M.; Nunes, M. R.; Costa, F. M. Structural and Morphological Characterization of $FeCo_2O_4$ and $CoFe_2O_4$ Spinels Prepared by a Coprecipitation Method. *Solid State Sci.* **2003**, *5*, 383−392.
(17) Sharma, Y.; Sharma, N.; Subba Rao, G. V.; Chowdari, B. V. R. Studies on Spinel Cobaltites, $FeCo_2O_4$ and $MgCo_2O_4$ as Anodes for Li-Ion Batteries. *Solid State Ionics* **2008**, *179*, 587−597.
(18) Mohamed, S. G.; Chen, C. J.; Chen, C. K.; Hu, S. F.; Liu, R. S. High-Performance Lithium-Ion Battery and Symmetric Supercapacitors Based on $FeCo_2O_4$ Nanoflakes Electrodes. *ACS Appl. Mater. Interfaces* **2014**, *6*, 22701−22708.
(19) Hu, L.; Zhong, H.; Zheng, X.; Huang, Y.; Zhang, P.; Chen, Q. $CoMn_2O_4$ Spinel Hierarchical Microspheres Assembled with Porous Nanosheets as Stable Anodes for Lithium Ion Batteries. *Sci. Rep* **2012**, *2*, 986−993.
(20) Balaish, M.; Kraytsberg, A.; Ein-Eli, Y. Realization of an Artificial Three-Phase Reaction Zone in a Li−Air Battery. *ChemElectroChem.* **2014**, *1*, 90−94.
(21) Landa-Medrano, I.; Pinedo, R.; de Larramendi, I. R.; Ortiz-Vitoriano, N.; Rojo, T. Monitoring the Location of Cathode-Reactions in Li-O_2 Batteries. *J. Electrochem. Soc.* **2015**, *162*, A3126−A3132.
(22) Sing, K. Reporting Physisorption Data for Gas/Solid Systems with Special Reference to the Determination of Surface Area and Porosity (Provisional). *Pure Appl. Chem.* **1982**, *54*, 2201−2218.
(23) De Koninck, M.; Poirier, S.-C.; Marsan, B. $Cu_XCo_{3-X}O_4$ Used as Bifunctional Electrocatalyst: Physicochemical Properties and Electrochemical Characterization for the Oxygen Evolution Reaction. *J. Electrochem. Soc.* **2006**, *153*, A2103−A2110.
(24) Xiao, J.; Kuang, Q.; Yang, S.; Xiao, F.; Wang, S.; Guo, L. Surface Structure Dependent Electrocatalytic Activity of Co_3O_4 Anchored on Graphene Sheets toward Oxygen Reduction Reaction. *Sci. Rep.* **2013**, *3*, 2300 DOI: 10.1038/srep02300.
(25) Fu, C.; Li, G.; Luo, D.; Huang, X.; Zheng, J.; Li, L. One-Step Calcination-Free Synthesis of Multicomponent Spinel Assembled Microspheres for High-Performance Anodes of Li-Ion Batteries: A Case Study of $MnCo_2O_4$. *ACS Appl. Mater. Interfaces* **2014**, *6*, 2439−2449.
(26) Mills, P.; Sullivan, J. A Study of the Core Level Electrons in Iron and Its Three Oxides by Means of X-Ray Photoelectron Spectroscopy. *J. Phys. D: Appl. Phys.* **1983**, *16*, 723.
(27) Qian, L.; Gu, L.; Yang, L.; Yuan, H.; Xiao, D. Direct Growth of $NiCo_2O_4$ Nanostructures on Conductive Substrates with Enhanced Electrocatalytic Activity and Stability for Methanol Oxidation. *Nanoscale* **2013**, *5*, 7388−7396.
(28) Hu, L.; Qu, B.; Li, C.; Chen, Y.; Mei, L.; Lei, D.; Chen, L.; Li, Q.; Wang, T. Facile Synthesis of Uniform Mesoporous $ZnCo_2O_4$ Microspheres as a High-Performance Anode Material for Li-Ion Batteries. *J. Mater. Chem. A* **2013**, *1*, 5596−5602.
(29) Alibeigi, S.; Vaezi, M. R. Phase Transformation of Iron Oxide Nanoparticles by Varying the Molar Ratio of Fe^{2+}:Fe^{3+}. *Chem. Eng. Technol.* **2008**, *31*, 1591−1596.
(30) Zhang, T.; Fan, H.; Liu, G.; Jiang, J.; Zhou, J.; Jin, Q. Different Effects of Fe^{2+} and Fe^{3+} on Conjugated Polymer $PPESO_3$: A Novel Platform for Sensitive Assays of Hydrogen Peroxide and Glucose. *Chem. Commun.* **2008**, 5414−5416.
(31) Xu, J. J.; Wang, Z. L.; Xu, D.; Zhang, L. L.; Zhang, X.-B. Tailoring Deposition and Morphology of Discharge Products Towards High-Rate and Long-Life Lithium-Oxygen Batteries. *Nat. Commun.* **2013**, *4*, 2438 DOI: 10.1038/ncomms3438.
(32) Zhang, K.; Zhang, L.; Chen, X.; He, X.; Wang, X.; Dong, S.; Han, P.; Zhang, C.; Wang, S.; Gu, L.; Cui, G. Mesoporous Cobalt Molybdenum Nitride: A Highly Active Bifunctional Electrocatalyst and Its Application in Lithium−O_2 Batteries. *J. Phys. Chem. C* **2012**, *117*, 858−865.
(33) Wang, Z.-L.; Xu, D.; Xu, J.-J.; Zhang, L.-L.; Zhang, X.-B. Graphene Oxide Gel-Derived, Free-Standing, Hierarchically Porous Carbon for High-Capacity and High-Rate Rechargeable Li-O_2 Batteries. *Adv. Funct. Mater.* **2012**, *22*, 3699−3705.

DOI: 10.1021/acsami.5b02180
ACS Appl. Mater. Interfaces 2015, 7, 12038−12046